




Enantiomorph conversion in single crystals of the Weyl semimetal CoSi

Wilder Carrillo-Cabrera¹, Paul Simon ¹, Marcus Schmidt¹, Markus König¹, Horst Borrmann¹, Aimo Winkelmann ², Ulrich Burkhardt ¹✉ & Yuri Grin¹

Chiral intermetallic phases may show unusual chemical and physical properties with non-trivial structure-property relationship. It is therefore of particular interest to study the structural conversion between domains of different handedness. Here, the atomic decoration of the enantiomorph exchange area within single crystal of the Weyl semimetal CoSi is determined by a combination of atomic-resolution scanning transmission electron microscopy imaging, single crystal X-ray diffraction and quantum chemical analysis of atomic interactions. Two-atomic [CoSi] units are shown to be the bonding base for the FeSi-type structure and may be considered as ‘pseudo-molecules’, thinking of molecular organic crystals. Tiny reorganisation of atomic interactions within these units results in the appearance of sequence ‘faults’ in the structure pattern i.e. in a different structural motif in the enantiomorph exchange area, which – contrary to the A and B enantiomorphs of CoSi – contains an inversion centre and allows a local enantiomorph ‘conversion’. Due to the special features of atomic interactions, the reorganisation of multi-atomic bonds leads to slightly higher total energy. This appears within one and the same grain which is prepared by the short distance chemical vapor transport.

¹Max-Planck-Institut für Chemische Physik fester Stoffe, Nöthnitzer Straße 40, 01187 Dresden, Germany. ²AGH University of Kraków, Academic Centre for Materials and Nanotechnology, al. A. Mickiewicza 30, 30-059, Kraków, Poland. ✉email: Ulrich.Burkhardt@cpfs.mpg.de

Materials having two states with different handedness, i.e. left- and right-handed have recently attracted a huge attention in the solid-state chemistry and physics due to their prospective to reveal novel properties. As for solid state physics, it was shown since the 80 s of the last century, that the intermetallic representatives of the FeSi (B20 in the *Strukturbericht* notation) structure type - MnSi and FeGe - show the Dzyaloshinskii-Moriya interaction which causes a modulation of the ferromagnetic structure as a consequence of the lack of inversion symmetry¹⁻⁵. The handedness of disilicide crystals induces spin polarization over macroscopic distances⁶. Appearance of non-collinear anti-ferromagnetism and anomalous Hall effect is also connected with the handedness of the crystal structures⁷. The handedness may be considered even as a quantum number for chiral phenomena on different scales of the matter⁸.

The left- and right-handed organic molecular enantiomers show in general similar but in details different properties, starting with the basic ones, like optical activity, i.e. polarisation rotation or circular birefringence⁹, via catalytical performance¹⁰ to biological activity¹¹. The transformation from one enantiomer into the other is called enantiomer conversion¹². For molecular enantiomers, this is usually a non-direct process, it requires several stages often including formation of diastereomers, solubility-assisted use of so-called receptors, e.g. for synthesis of amino acids with given handedness¹³, solid-state conversion of stereoisomers¹⁴ or enantio-convergent catalysis on a chiral catalyst¹⁰.

Coming to the solids, the conditions for formation of left- and right-handed molecular crystals, i.e. the symmetry conditions under which such crystal structure can or cannot be chiral, are currently under debate¹⁵. In particular, the systems with the space group $P2_13$, among others, have recently been discussed in detail^{16,17}. The formation of molecular crystals with different handedness seems to be based on interplay between the symmetry of the molecule and the conditions of crystallization. The left- and right-handed structures can be formed by chiral and achiral molecules. If such a crystal has the symmetry of a Sohncke space group, the crystal structure is chiral¹⁷. Not very much is known about the enantiomorph conversion within such crystals.

The same conditions should be valid for inorganic crystals. The historically known example of enantiomorph materials is quartz. Its enantiomorph structures are formed by achiral building units - $[\text{SiO}_4]$ tetrahedra. Interestingly, here the low-temperature (α -quartz) and high-temperature (β -quartz) modifications of the compound belong to the chiral pairs of Sohncke groups $P3_121$ ($P3_221$) and $P6_222$ ($P6_422$), respectively. This temperature-driven $\alpha \leftrightarrow \beta$ phase transformation - called quartz inversion - may reveal a handedness change similar to the enantiomorph conversion. Structurally, it involves a rotation of the tetrahedra with respect to each other without changing their linkage¹⁸. This leads to a volume change during the transition and usually results in the cracking of single crystals and bulk (ceramic) materials containing quartz. This handedness change is discussed as one of the reasons for damages and reactions in the earth crust¹⁹. The real enantiomorph conversion is observed in quartz twins¹⁸. While difference in the properties of the molecular enantiomorphs or enantiomorph molecular crystals is already described in the literature, the properties of the solid enantiomorphs, in particular intermetallic ones are still under debate.

The intermetallic representatives of the FeSi structure type attracted quite early a large attention due to the wide spectrum of interesting physical properties^{20,21}. Some representatives of the FeSi type were shown to belong to the so-called Weyl semimetals due to the symmetry of their crystal structure yielding multifold

degenerate band crossings with large *Chern* numbers²². Among them, cobalt monosilicide CoSi attracted the most attraction²³⁻²⁵.

The crystal structure of the FeSi type can be derived from the NaCl one (Supplementary Note S1) and belongs to the Sohncke-type cubic space group $P2_13$, i.e. there exist two enantiomorph forms, called A and B²⁶, which - in contrary to quartz - belong to the same space group. The assignment of the enantiomorph for such materials was usually made by a full crystal structure determination, employing the Flack-Bernardinelli strategy for the definition of the absolute structure^{27,28}. A recent study using the electron backscatter diffraction (EBSD) method, demonstrated that the absolute structure of CoSi crystals (grown by chemical vapour transport, CVT) was correctly assigned and confirmed by single crystal X-ray structure refinement²⁹. Further investigation of CoSi crystals prepared by the micro CVT (mCVT, cf. Methods) revealed the presence of both enantiomorphs within one and the same single crystalline grain (crystallite). Similar behaviour was recently observed in CoSi nanowires^{30,31}. The purpose of the present study is the determination of the atomic structure of the border region between the enantiomorphs.

Results

EBSD and XRD investigations. Single crystals and agglomerates of CoSi (inset Fig. 1a) were grown via micro chemical vapour transport, embedded into a conductive resin, crosscut and polished (cf. Methods). Most of the crystallites are formed by two or more grains which show significant orientation contrast in the SEM images (Fig. 1a). The selected crystallite 1 (red circle in Fig. 1a) reveals grains in three crystallographic orientations, the largest one oriented approximately along $[100]$ (Fig. 1b). EBSD pattern simulations accounting for dynamical electron scattering and its comparison with experiment by a full pattern matching approach^{29,32} allows to assign the absolute structure of A and B enantiomorph forms of the FeSi (B20)-type structure to the different grains. The A- and B- forms are defined according to the values of the coordinates for the Co and Si, both in the Wyckoff site $4(a)$ xxx : for the A form $x(\text{Co}) \approx 0.15$ and $x(\text{Si}) \approx 0.85$, for the B form $x(\text{Co}) \approx 0.85$ and $x(\text{Si}) \approx 0.15$ ^{26,29}.

Somehow unexpected, regions with different absolute structure were observed within one and the same single grain (Fig. 1c). For the verification of the assignment, three specimens of ca. $20 \mu\text{m}$ size were cut from the grain by focused ion beam (FIB) technique (Fig. 1d), employing the enantiomorph distribution map from electron back scatter diffraction (EBSD), and subjected to the single crystal X-ray diffraction experiment (XRD) (Supplementary Note S2).

The refinement of the crystal structure using single-crystal X-ray diffraction data shows - in full agreement with the EBSD information - the FeSi-type form A for the crystal 1 and FeSi-type form B for the crystal 2. The assignment is confirmed by the lower residual values for the correct absolute structure (cf. $R_F = 0.0144$ for the form A and $R_F = 0.0311$ for the form B in case of the crystal 1) and the values of the Flack parameter being close to zero for the correct form for both crystals (Supplementary Table S2). These results are in full agreement with the previous study on enantiomorphs in CoSi²⁹. The structure refinement for crystal 3 yields the lowest residual values obtained applying the model of inversion twinning, i.e. assuming the presence of both forms in the same single crystal with full overlap of their diffraction reflections, well in agreement with the EBSD characterization of the crystals before lift-out. The refinement yields the volume A/B ratio of 0.655 to 0.345 (Supplementary Table S2). This result as such is not rare for crystal structure refinements in general, the inversion twin model allows often to

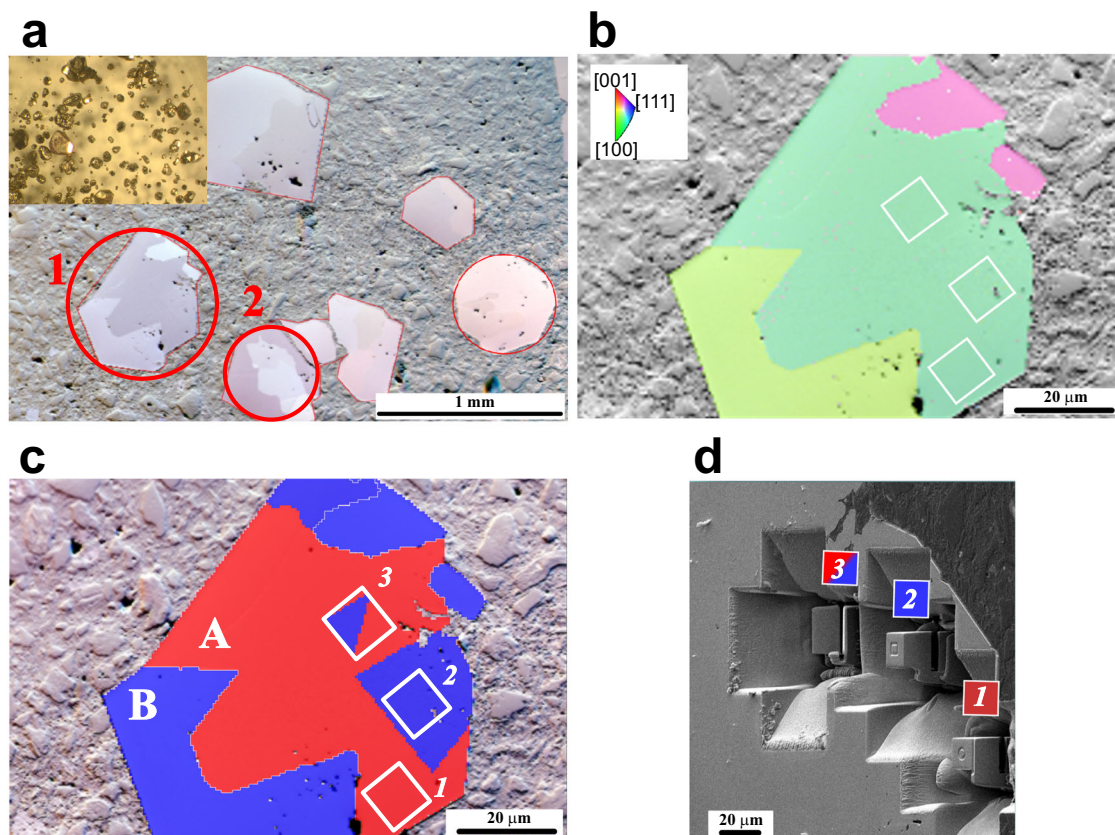


Fig. 1 Microstructure of polycrystalline CoSi. **a** Microstructure of the mCVT-prepared crystallites of CoSi pictured with the fore-scattered electron detector; (inset): irregular shaped, partly agglomerated CoSi crystallites (light optical image). **b** Inverse pole figure z (IPFz) of crystallite 1; (inset): color code of the unit cell direction perpendicular to the sample surface; **c** enantiomorph distribution map with areas assigned to the A- form (red) and B- form (blue); **d** FIB-cut areas (white squares) of the single crystals 1, 2, and 3 used for single crystal X-ray diffraction.

reduce the residuals. In the present case, this observation overlaps with the fact, that specimen 3 was cut out from the region of the initial single crystalline grain, which a priori includes an enantiomorph exchange border. This finding raised the question about atomic decoration of this border, which would allow a mutual ‘conversion’ of absolute structures by preserving the geometry of the diffraction pattern. This situation was successfully resolved applying high-resolution scanning transmission electron microscopy (HR-STEM).

HR-STEM investigations. For this study, the EBSD characterization was performed on crystallite 2 (Fig. 1a), which is built up by several grains with different crystallographic orientation (cf. Supplementary Note S3). For the grain with its surface almost perpendicular to [001] direction, two domains of the B form of the CoSi are found to be separated by a slab of the A form with approx. 30 μm width (Fig. 2 and Supplementary Figure S3). Three lamellae that include the A|B boundary were cut by the FIB technique with different tilt angle for the TEM and STEM investigations (Supplementary Note S4) along the zone axes $[00\bar{1}]$, $[10\bar{1}]$ and $[101]$. The A|B region appears in the TEM image as a straight, dark line perpendicular to the surface (Fig. 3). It allows the clear relation of the boundary in the TEM images and the EBSD-determined handedness of the domains on the sample surface.

At low magnification in the TEM image along $[10\bar{1}]$ (Fig. 3a), the enantiomorph exchange region in CoSi is visible only at the thinner top (ca. 20 nm) of the specimen due to small internal stresses (Fig. 3a). The brightness contrast in the TEM images fades with increasing thickness of the sample material. Also, the

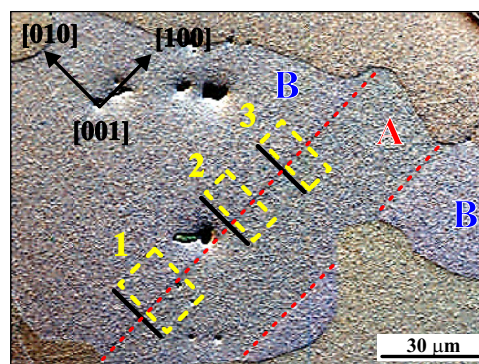


Fig. 2 Microstructure of the twinned CoSi crystallite. Scanning electron micrograph (fore-scattered electron detector) of the CoSi crystallite 2 (Fig. 1a). The grain with (001) orientation (bluish) is formed by two domains of the B-form separated by the section of the A- form (s.a. Supplementary Figure S3). FIB cut areas 1, 2, and 3 (dashed yellow rectangles) for preparing lamellae for the TEM studies along the zone axes $[00\bar{1}]$, $[101]$ and $[10\bar{1}]$, respectively. The black lines represent tops of protection platinum layers. These areas are located along one of the two absolute structure exchange areas. The enantiomorph exchange regions (red dashed lines) can be recognized due to the small differences in crystal morphology as a result of metallographic finishing.

resolution of the HR-TEM image (Fig. 3b) was relatively low, so that the image does not allow the atomic decoration using the crystal structure projection, mostly due to multi-beam dynamical effects that affect the modules and phases of the diffracted

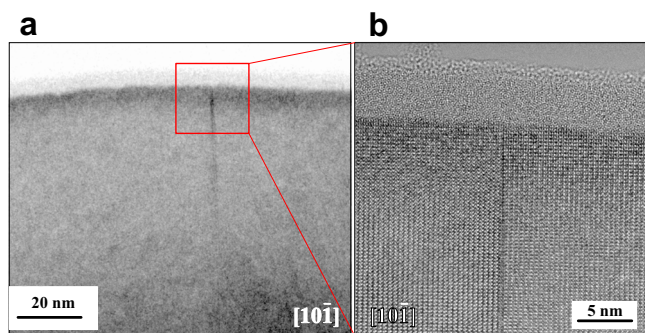


Fig. 3 CoSi enantiomorph exchange area (TEM images). Low-resolution TEM (a) and high-resolution HR-TEM (b) images of the enantiomorph exchange area (prepared from area 3 in Fig. 2).

intensities which yield a TEM image (Supplementary Figure S4). Therefore, most of our present results are based upon HR-STEM imaging using a high-angle annular dark-field (HAADF) detector. The annular dark-field HR-STEM images are less sensitive to sample thickness and have atomic number-dependent contrast ($\sim Z^2$) allowing clear identification of Co and Si columns. Co-dominated columns are represented by well localized, bright spots, while Si-dominated columns are less bright, less localized and appear in the images due to the brightness colour coding as yellowish, blurred spots (Fig. 4). The atomic-resolution STEM HAADF images in three crystallographic directions (Fig. 4) show the periodicity of 4.45 Å along [010], which is consistent with the EBSD-based orientation of the (010) plane, being parallel to the enantiomorph exchange region. The images on the left and the right sides of each panel can be easily understood as the pristine matrix of the CoSi B and A forms, respectively (cf. light blue- and red-marked unit cells), as this is established by EBSD on the microscale level. The striking difference is visible in the middle part of each image. Overlaying of the image with the projection of the crystal structures of both enantiomorphs, one recognizes that in the middle region the A and B lattices do not match (bottom part of each panel in Fig. 4). A shift of $\Delta \approx 0.2a_{\text{CoSi}}$ parallel to [100] appears between the lattices of the A- and B- form (all three panels). The arrangement of the atomic columns in this region is not found in the regular A- or B-form regions.

Discussion

Chemical bonding analysis. By combined analysis of the images, a model for the enantiomorph exchange region was derived (Supporting Note S5). It has the symmetry of the centrosymmetric monoclinic space group $P2_1/c$.

For simplification of the calculations, a relatively small model was constructed with a unit cell ($a = a_{\text{cub}}$, $b = a_{\text{cub}}$, $c = 4a_{\text{cub}}$) containing one unit cell of the A and B form each, together with two unit cells of a new motif, which can be understood as a kind of stacking variation of the FeSi-type one (Supplementary Note S5). Striking feature of this model is the presence of the inversion centre in the latter slabs. This inversion centre originates from a different centrosymmetric structural arrangement, similar to the KHg-type one (cf. Supplementary Note S6). In contrary, the $P2_1/c$ model (Supplementary Table S5-6) used for the interpretation of the enantiomorph exchange region represents a structure type, which up to our best knowledge is not realized in any binary system. The HR-STEM images close to the enantiomorph transition region can be completely understood using the central inversion-centre containing part of the $P2_1/c$ model (unit cell of $P2_1/c$ model in yellow, top region of each panel in Fig. 4 and Supplementary Figures S5-1, S5-2), which continuously turns into

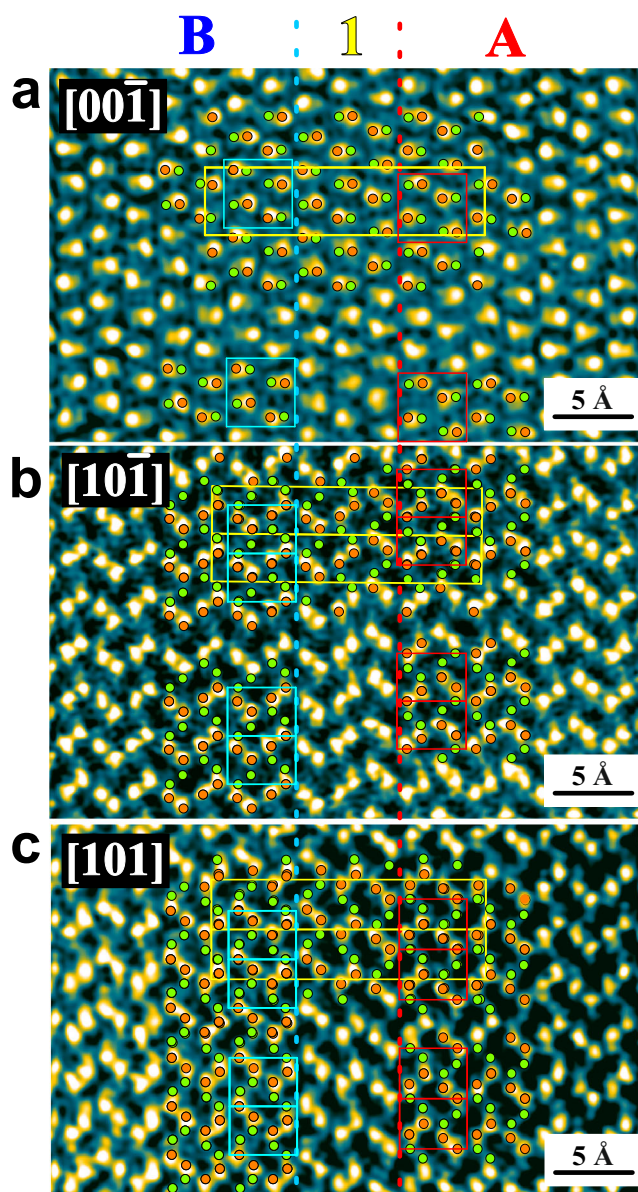


Fig. 4 CoSi enantiomorph exchange area (HR-STEM images). Aberration-corrected STEM images (HAADF) of the enantiomorph exchange area (yellow 1) in the CoSi crystallite 2 (Fig. 2) as viewed along the direction (a) [00 $\bar{1}$], (b) [10 $\bar{1}$], (c) [101]. The images are superimposed with the structure models of CoSi form B (unit cell - light blue), CoSi form A (unit cell - red) and $P2_1/c$ model (unit cell - yellow, Co - orange, Si - green). The coordinate system of Fig. 2 is used, the [010] direction is horizontal to the left in all three panels.

the A- and B-type pattern on both sides (unit cells in red and light blue, respectively, top region of each panel in Fig. 4).

Formation of a different structural pattern in the region between the enantiomorphs in CoSi within the same crystallite resembles the observation of phasoids found earlier (also by HR-TEM) in the ternary oxide systems - intergrowth tungsten bronzes³³⁻³⁵. Similar to the phasoids, the structural pattern of the enantiomorph exchange area is not found as an independent chemical object (compound). In contrast to the latter, the phasoids were found to be more extended and the presence of a symmetry element of the second kind (mirror plane or inversion centre) is not a necessary feature of phasoids.

The understanding of atomic interactions in the FeSi-type structure arrangement helps to shed light on the appearance of the enantiomorph exchange area. Chemical bonding analysis in the isotypic compound GaPd indicated already the quasi two-atomic Ga-Pd bonding with essential tendency to enhance the atomicity (as it was shown by analysis of the three-centre delocalization indices)³⁶. Evaluation of the electron density in CoSi forms A and B, within the QTAIM framework²⁰, shows charge transfer according to $\text{Si}^{+0.54}\text{Co}^{-0.54}$, being similar to the reported one for $\text{Ga}^{+0.5}\text{Pd}^{-0.5}$ ³⁶. Due to the enantiomorph relation of both forms, the QTAIM shapes of the Co and Si atoms in the A and B forms are enantiomorph to each other (Supplementary Figure S7-1).

Application of the electron localizability approach in the chemical bonding analysis in position space³⁷ to CoSi reveals only two types of bonds in this compound (Figure 5 for the form A and Supplementary Fig. S7-2 for the form B), both are four-atomic involving one silicon and three cobalt atoms each. The first one has its attractor on the three-fold axis (red bond basin, Fig. 5c, d and Supplementary Fig. S7-2), the second one interlinks the atoms along the shortest Si-Co bond on the three-fold axes (yellow, orange, and pink basins in Fig. 5 and supplementary Fig. S7-2). These four (1 + 3) basins together form a ‘super-basin’ with six characteristic plane faces (3 of enantiomorph form L + 3 of enantiomorph form R, turquoise margin line in Fig. 5 and Supplementary Fig. S7-2). In CoSi form A, the R faces are closer to the Si core, the L faces - to the Co core (Fig. 5c, d), in CoSi form B, the L faces are closer to the Si core and the R faces - to the Co core (Supplementary Fig. S7-2). In combination with the enantiomorph shapes of the QTAIM atoms (Supplementary Figure S7-1), this makes up the enantiomorphism in the FeSi-type structure from the bonding representation. The super-basins fill-up the volume of the unit cell in the ELI-D representation (except spherical atomic core regions), using the plane faces R and L as contact surfaces.

Thus, from the bonding point of view, the basic building block of the structure is the polar two-atomic Co-Si unit. In projection along [100], such units form the characteristic zigzag patterns in both enantiomorph forms of CoSi (Fig. 5g, h), which are also recognizable in the HR-STEM HAADF images, if connecting pairwise the spots with different intensity (Fig. 4a).

The two-atomic Co-Si units are also present in the models of the enantiomorph exchange area. While in the peripheral regions their zigzag-like arrangement agrees with that in the A and B forms of CoSi, in the middle region a kind of sequence ‘fault’ appears (Fig. 6a). Analysis of the ELI-D distribution reveals three types of super-basins. Two of them are equivalent to the one observed in the A and B forms of pristine CoSi (Fig. 6d), if comparing the shape and the atomicity of the bond basins. The third one (Fig. 6b) reveals redistribution in the atomicity (3a-SiCo₂ and 5a-SiCo₄ bonds appear instead of two 4a-SiCo₃ ones). This results in the appearing of the achiral planar faces A together with L and R ones in the shape bond super-basin. In the enantiomorph exchange area, such basin is condensed to the two others via available R and L faces (Fig. 6c). The re-organisation of R and L faces in the shape allows the new way of super-basins condensation and the appearance of above-mentioned sequence ‘fault’ in the enantiomorph exchange area. Such bond reorganisation costs energy. The $P2_1/c$ model of enantiomorph exchange area shows 1 mHa per f.u. higher total energy in comparison to the pristine CoSi.

Conclusion

Summarizing, the combined employment of high-resolution STEM HAADF imaging, single crystal X-ray diffraction, and

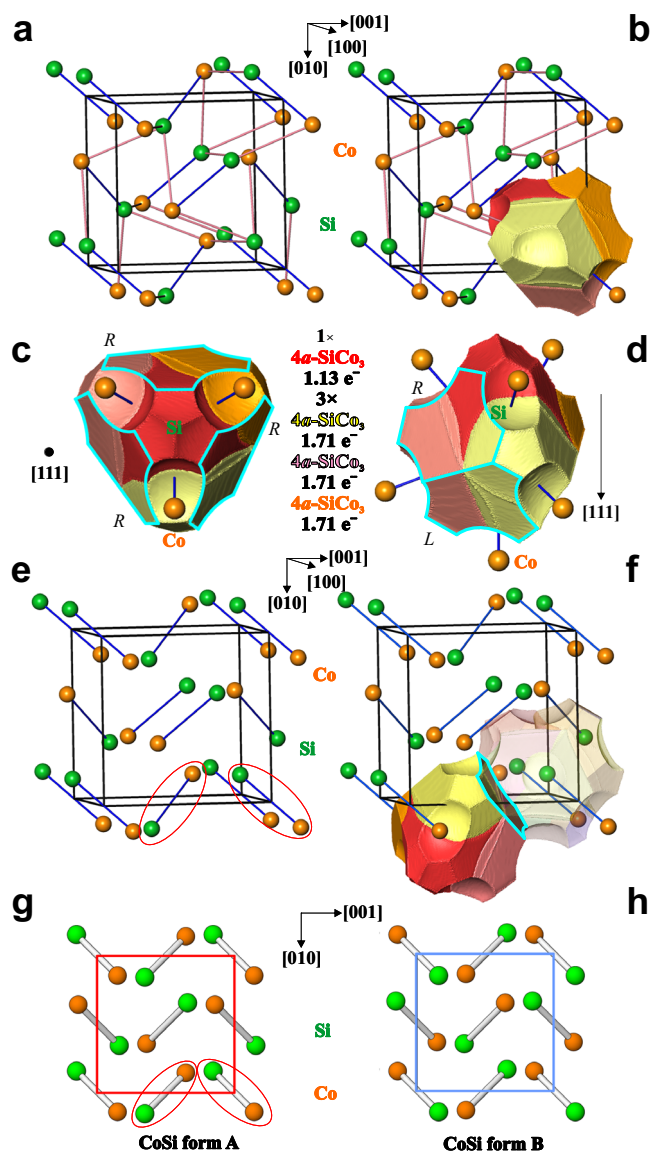


Fig. 5 Chemical bonding in CoSi. **a** Unit cell of the A form with the interatomic distances $< 2.4 \text{ \AA}$. **b** Positions of the ELI-D bond basins of the four-atomic bonds around the shortest Co-Si contact of 2.31 \AA (blue). **c, d** Arrangement and electronic populations of ELI-D bond basins along [111] and perpendicular to [111]; yellow, pink and orange bond basins are symmetry equivalent; R and L types of plane faces of the bond super-basin are outlined in turquoise. **e** Unit cell of the A form with the shortest distances of 2.31 \AA in the Co-Si pairs. **f** ELI-D bond basins around two neighbouring Co-Si units. **g, h** Schematic representations of the A and B forms of CoSi by basic bonding blocks - Co-Si pairs.

quantum chemical analysis of chemical bonding allowed to establish the atomic decoration of the enantiomorph exchange area within a single crystal of the Weyl semimetal CoSi. Slight reorganisation of atomic interactions within the two-atomic [CoSi] units, which may be considered as ‘pseudo-molecules’ (cf. molecular crystals in the Introduction), leads to the sequence ‘faults’ in the structure pattern i.e. to an appearance of different structural motifs in the enantiomorph exchange area, including an inversion centre. The segment containing inversion centre is completely described in term of the space group, unit cell parameters, and atomic coordinates of a hypothetical crystal structure showing only the features characteristic for the central part of enantiomorph exchange region, inclusive its similarity to the

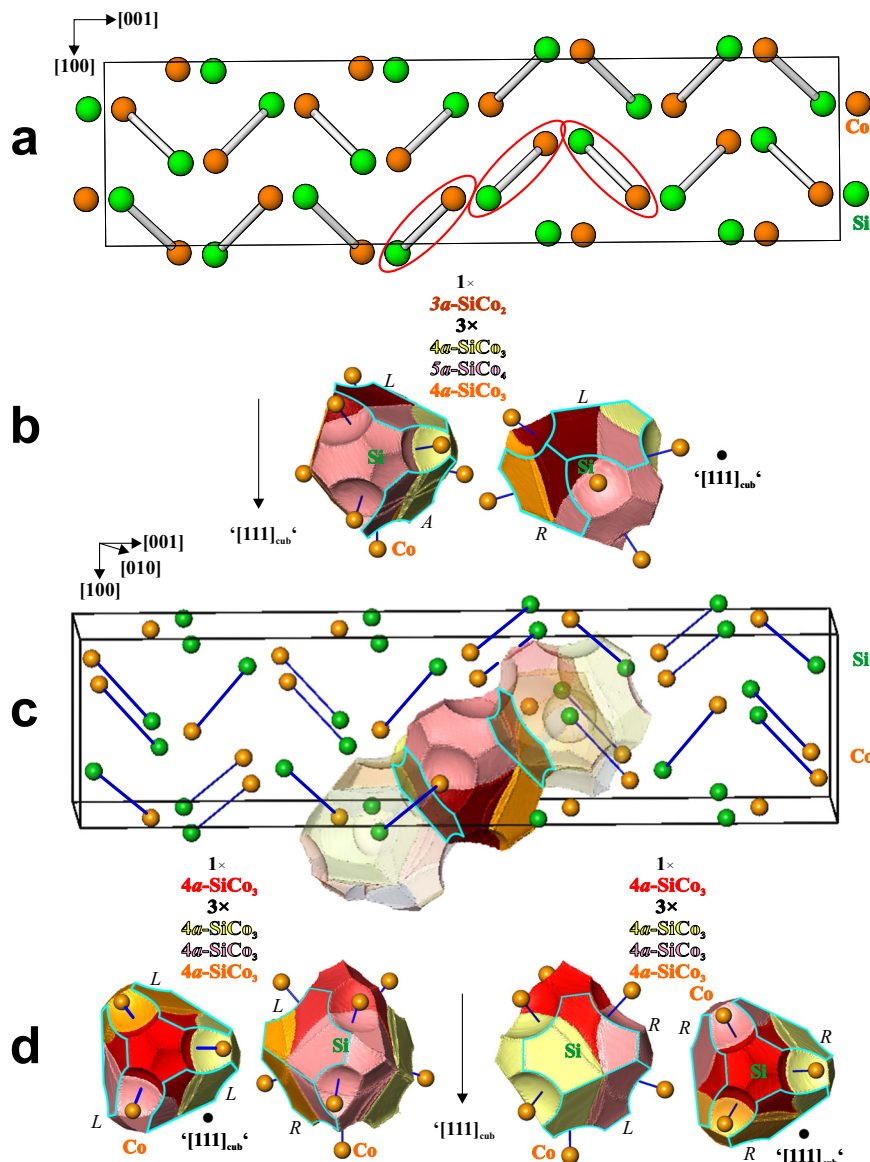


Fig. 6 Chemical bonding within the enantiomorph exchange area in CoSi. **a** Schematic representation of the monoclinic structure model (Supplementary Table S5-6) by basic bonding blocks – Co-Si pairs. The enantiomorph exchange region with the sequence ‘fault’ emphasized by red marks. **c** Unit cell of the monoclinic structure model with the shortest Co-Si contacts (blue), and interconnection of three bond super-basins in the enantiomorph exchange area (red marks in the top panel). **b, d** Bond super-basins in projection along and perpendicular to pristine cubic [111] direction; the colours of bond basins are equivalent to Fig. 5; R, L and A types of plane faces of bond super-basins are outlined in turquoise.

known structure type KHg (cf. supplementary note S6). The presence of this segment allows the local conversion of the enantiomorphs. The recently proposed model for the atom arrangement near the (001) plane of the merohedral twin boundary identified in CoSi nanowires^{30,31} contains an inversion center, too. Detailed analyses by DFT calculation³¹ indicate that the occurrence of the inversion centre should have detectable influence on the transport properties of the merohedrally twinned CoSi nanowires. It is reasonable to assume similar effects in the concrete change from to A- to the B- form along the [010] direction in CoSi bulk materials prepared by mCVT. Slightly higher total energy of the system in this region allows to understand, why the enantiomorph conversion can appear during mCVT preparation within the same single crystal. During the crystallization process, some atomic arrangements may form already in the crystallization medium, e.g. gold nanoparticles in liquid phase, but they also may change during the formation of

the crystallization front on the phase border³⁸. Furthermore, due to the reorganisation of multi-atomic bonds, the volume of the bond super-basins in the two-atomic unit [CoSi] practically does not differ between the enantiomorph-only and enantiomorph-exchange regions. Thus, the enantiomorph conversion may proceed without volume increase, in contrary to the $\alpha \leftrightarrow \beta$ transformation in quartz^{18,19}, where a rotation of the covalently bonded SiO₄ tetrahedra without changing the linkage is necessary for enantiomorph conversion.

Methods

Preparation of single crystals. Single crystals of CoSi were grown via micro chemical vapour transport (mCVT) using iodine as a transport agent^{39,40}. In the initial step, CoSi was synthesized by isothermal reaction of the elemental cobalt (powder Alfa Aesar 99.998%) and silicon (powder Alfa Aesar 99.999%) in the presence of iodine (Alfa Aesar 99.998%) at 700 °C in evacuated fused

silica tubes during 120 h. In an additional step, CoSi was recrystallized during 3 weeks by a chemical transport in a very small temperature gradient (5 – 10 K) close to 700 °C, and a transport agent concentration of 0.5 mg/cm³ iodine (Alfa Aesar 99.998%). In this special type of chemical transport reaction also known as short distance transport, crystallization takes place via the gas phase by microdiffusion in a small temperature gradient (same degrees) over a short distance. The limiting case is the re-crystallization or mineralization of the source material or as in the present case, that the crystals grow on the source material. Polished cross-sections of agglomerated crystals were prepared by a metallographic technique and, after SiO₂ finishing, allowed to record high-quality EBSD patterns. In almost all cases, the CoSi crystallites prepared by this process consist of several differently oriented grains, which can usually be recognized by the fact that the outer shape has re-entrant edges. Typically, both handedness are represented, so that at least one grain has a handedness different from the majority. The crystallites shown in Figs. 1, 2 and Supplementary Fig. S3 are typical representatives where in at least one grain a twinning occurs which is associated with a change of handedness.

Single-crystal X-ray diffraction. The cubic specimens (size 40 μm) were investigated on a Rigaku AFC-7 diffraction system equipped with a Saturn 724 CCD detector using the MoK α radiation ($\lambda = 0.71073$ Å). The absorption correction of the reflection intensities was performed by multi-scan routine⁴¹ in the Laue class *m*3. All crystallographic calculations were performed with the program packages WinCSD⁴² and SHELX⁴³. The results and experimental details are summarized in Supplementary Table S2.

Electron backscatter diffraction. The experimental electron backscatter diffraction patterns were acquired using an EBSD system (Bruker Nano, Berlin, Germany) attached to a scanning electron microscope JSM7800 F (Jeol). All measured Kikuchi patterns were saved for post-processing using custom data analysis software (Esprit Vers. 2.3, Bruker Nano). The quantitative comparison between the experimental and the simulated pattern of the A- and B- form of the CoSi phase is based on the cross-correlation values r_A and r_B with higher r -value ($0 \leq r \leq 1$) for a better match⁴⁴. The consideration of dynamical electron scattering leads to significant differences in the simulated patterns of A- and B- form. A best-fit pattern matching approach for each experimental pattern was used to assign the orientation and the chirality. The evaluation of the complete mapping provides the grain orientation map and the distribution of both enantiomorphs in the polycrystalline material. For more details see Ref. ^{29,32}.

FIB preparation for X-ray diffraction and TEM studies. X-ray diffraction data sets were collected using single crystal cubes (size 40 μm) which were cut out from polycrystalline material by the focused ion beam technique employing a FEI Helios G4 PFIB machine (60 nA, 30 kV Xe-beam).

For the high-resolution scanning transmission electron microscopy (HR-STEM) study, focused ion beam (FIB) thin lamellae were machined by use of a FEI Quanta 200 3D ion/electron dual beam device (FEI Company, Eindhoven, Netherlands) equipped with an Omniprobe micro-manipulator. All selected areas for FIB sectioning were positioned perpendicular to a (010) twin boundary. For the FIB lamellae fabrication, first, the selected areas (black lines on yellow rectangles positioned perpendicular to the (010) twin boundary on the polished crystal in Fig. 2) were covered with protective platinum layers (2 μm thickness),

applying an acceleration voltage of 30 kV and a current of 0.1 nA. Second, the oriented 2 μm thick FIB cross-sections were cut of the twinned crystal area by the lift-out technique⁴⁵ and after being transferred to molybdenum half-rings were further thinned down to electron transparency to a thickness of about 40 nm, using an acceleration voltage of 30 kV and currents of 3 – 0.1 nA. In the final stage, the FIB cuts were polished to a thickness of about 20 nm by applying a low acceleration voltage of 5 kV and a current of 0.3 nA. It should be mentioned that the defined crystallographic alignment of the FIB cuts could be successfully realized because of the previous knowledge of the crystal orientation determined by the EBSD method²⁹. Also, because the required cross-sections were inclined to the sample surface, after deposition of the protecting Pt layer, the polished sample was rotated to different angles before FIB cross-section manufacturing (to $\sim -35^\circ$ for [101] cut and to $\sim 55^\circ$ for [10 $\bar{1}$] cut). For the most inclined [00 $\bar{1}$] FIB case, a nearly cubic fragment ($\sim 20 \times 20 \times 20$ μm) was manufactured in several stages, first extracted, rotated 90°, transferred to a molybdenum half-ring, covered with a Pt layer, further rotated $\sim 10^\circ$, manufactured to a 2 μm thin FIB cut, and moved to another molybdenum half-ring for final thinning (s.a. Supplementary Note S4).

High-resolution scanning transmission electron microscopy.

Preliminary, the exact orientation of the FIB lamellae and position of the twin interface was checked by conventional TEM analysis carried out by the FEI Tecnai F30-G² with Super-Twin lens (FEI) with a field emission gun at an acceleration voltage of 300 kV. The point resolution amounted to 2.0 Å, and the information limit amounted to about 1.2 Å. The microscope is equipped with a wide angle slow scan CCD camera (MultiScan, 2k × 2k pixels; Gatan Inc., Pleasanton, CA, USA).

The HR-STEM analyses of the FIB samples were performed on the double-corrected JEM-ARM300F electron microscope at 300 kV (Dresden Grand ARM, JEOL Company). The spherical aberration (C_s) of the condenser and the objective lens are corrected by dodecapole correctors in the beam (STEM) and in the image (TEM) forming system. The HR-STEM images were taken with a HAADF detector. The STEM resolution for the dark-field modus is 0.5 Å. All of the HR-STEM images reproduced in this article were Fourier filtered applying a band-pass mask (Gatan Digital-Micrograph software). The STEM image linear distortions (produced by specimen and stage drift during image acquisition) were corrected with the software tool STEM SI Warp⁴⁶, which was inserted as a plugin in Digital-Micrograph software.

High-resolution TEM analyses (TEM resolution about 0.7 Å) were also performed but due to dynamical multi-beam effects the TEM images did not correspond to the real structure. Lamellar CoSi samples much thinner than 20 nm are necessary for better TEM images. Therefore, we performed mainly a HR-STEM study, which in general results in better images for ~ 20 nm thin FIB samples. However, for the [10 $\bar{1}$] case, the HR-TEM image of a narrow region at the top of the FIB lamella was acceptable (cf. Supplementary Fig. S4).

Quantum chemical calculations. Electronic structure calculations and chemical bonding analysis were carried out employing the all-electron, full-potential method local orbital (FPLO) within the local density approximation⁴⁷ and the Perdew-Wang parametrization⁴⁸. The structures of A, B forms, the model of the enantiomorph conversion region as well as the hypothetical centrosymmetric *cs*-CoSi were optimized prior to further calculations. Because the Co-Si unit plays the key role in the structural arrangement, the total energy is calculated for one formula unit (f.u.) CoSi which allows to compare all the models above, which

have different amounts of formula units per unit cell. For comparison of the models with different numbers of formula units in the unit cells, we use the value of total energy difference per formula unit CoSi, i.e. $\Delta E_{\text{fu}} = E(\text{total})_{n_{\text{fu}}^{-1}} - E(\text{total})_{\text{cub}}/4$, where n_{fu} is the number of formula units per unit cell in the analyzed model. The energy difference on the level of mHa are considered as large and lead, in general, to the energetical unfavourability.

For the analysis of the chemical bonding in direct space the electron density and the electron localizability indicator ELI-D were calculated⁴⁹ with a module implemented in the program package⁵⁰. The computed distributions of ELI-D and electron density were analysed with the program DGrid⁵¹. For this purpose, the electron density was integrated within so-called basins, i.e., space regions confined by zero-flux surfaces of the gradient field. This technique follows the procedure proposed in the Quantum Theory of Atoms in Molecules (QTAIM⁵²) and provides electron counts for the basins of atoms (QTAIM populations of the atoms) and bonds (bond populations). The combined analysis of electron density and ELI-D constitutes a basis for the description of chemical bonding^{37,53}, especially in intermetallic compounds^{54,55}.

Data availability

All data needed to evaluate the conclusions in the paper are present in the paper and/or the Supplementary Materials. Full sets of supplementary crystallographic data as well as raw and evaluated EBSD data for this paper are available on request from the authors.

Received: 26 June 2023; Accepted: 30 November 2023;

Published online: 19 December 2023

References

- Bak, P. & Jensen, M. H. Theory of helical magnetic structures and phase transitions in MnSi and FeGe. *J. Phys. C: Solid State Phys.* **13**, L881 (1980).
- Pfleiderer, C., McMullan, G. J., Julian, S. R. & Lonzarich, G. G. Magnetic quantum phase transition in MnSi under hydrostatic pressure. *Phys. Rev. B* **55**, 8330–8338 (1997).
- Doiron-Leyraud, N. et al. Fermi-liquid breakdown in the paramagnetic phase of a pure metal. *Nature* **425**, 595–599 (2003).
- Pfleiderer, C. et al. Partial order in the non-Fermi-liquid phase of MnSi. *Nature* **427**, 227–231 (2004).
- Moskvin, E. et al. Complex chiral modulations in FeGe close to magnetic ordering. *Phys. Rev. Lett.* **110**, 077207 (2013).
- Shiota, K. et al. Chirality-induced spin polarization over macroscopic distances in chiral disilicide crystals. *Phys. Rev. Lett.* **127**, 126602 (2021).
- Kübler, J. & Felser, C. Non-collinear antiferromagnets and the anomalous Hall effect. *Europhys. Lett.* **108**, 67001 (2014).
- Felser, C. & Gooth, J. Topology and chirality. *arXiv* **2205**, 05809 (2022).
- Shu-Kun L. *Molecules*. 4th edn. (ed. Francis A. Carey). Vol. 5 (Kluwer Academic, 2000).
- Mohr, J. T., Moore, J. T. & Stoltz, B. M. Enantioconvergent catalysis. *Beilstein J. Org. Chem.* **12**, 2038–2045 (2016).
- Drayer, D. E. Pharmacodynamic and pharmacokinetic differences between drug enantiomers in humans: an overview. *Clin. Pharmacol. Ther.* **40**, 125–133 (1986).
- Baer, E. & Fischer, H. O. Conversion of D (+)-acetone glycerol into its enantiomorph. *J. Am. Chem. Soc.* **67**, 944–946 (1945).
- Fu, R., So, S. M., Lough, A. J. & Chin, J. Hydrogen bond assisted l to d conversion of α -amino acids. *Angew. Chem. Int. Ed.* **59**, 4335–4339 (2020).
- Engwerda, A. H. J. et al. Solid-phase conversion of four stereoisomers into a single enantiomer. *Angew. Chem. Int. Ed. Engl.* **57**, 15441–15444 (2018).
- Gautier, R., Klingsporn, J. M., Van Duyne, R. P. & Poepfelmeier, K. R. Optical activity from racemates. *Nat. Mater.* **15**, 591–592 (2016).
- Rekis, T. Comment on the article Symmetry and chirality in crystals. *J. Appl. Crystallogr.* **56**, 322–323 (2023).
- Nespolo, M. Molecular versus structural chirality. *J. Appl. Crystallogr.* **56**, 44–47 (2023).
- Nesse WD. *Introduction to Mineralogy*, 3 edn (Oxford Univ. Press, 2016).
- Johnson, S. E., Song, W. J., Cook, A. C., Vel, S. S. & Gerbi, C. C. The quartz $\alpha \leftrightarrow \beta$ phase transition: Does it drive damage and reaction in continental crust? *Earth Planet. Sci. Lett.* **553**, 116622 (2021).
- Pedrazzini, P. et al. Metallic state in cubic fege beyond its quantum phase transition. *Phys. Rev. Lett.* **98**, 047204 (2007).
- Wilhelm, H. et al. Precursor phenomena at the magnetic ordering of the cubic helimagnet FeGe. *Phys. Rev. Lett.* **107**, 127203 (2011).
- Bradlyn, B. et al. Beyond Dirac and Weyl fermions: unconventional quasiparticles in conventional crystals. *Science* **353**, aaf5037 (2016).
- Rao, Z. et al. Observation of unconventional chiral fermions with long Fermi arcs in CoSi. *Nature* **567**, 496–499 (2019).
- Schröter, N. B. M. et al. Observation and control of maximal Chern numbers in a chiral topological semimetal. *Science* **369**, 179–183 (2020).
- Takane, D. et al. Observation of chiral fermions with a large topological charge and associated fermi-arc surface states in CoSi. *Phys. Rev. Lett.* **122**, 076402 (2019).
- Spence, J. C. H., Zuo, J. M., O’Keeffe, M., Marthinsen, K. & Hoier, R. On the minimum number of beams needed to distinguish enantiomorphs in X-ray and electron diffraction. *Acta Crystallogr. Sect. A* **50**, 647–650 (1994).
- Flack, H. D. & Bernardinelli, G. Absolute structure and absolute configuration. *Acta Crystallogr. Sect. A* **55**, 908–915 (1999).
- Flack, H. D. Chiral and achiral crystal structures. *Helv. Chim. Acta* **86**, 905–921 (2003).
- Burkhardt, U. et al. Absolute structure from scanning electron microscopy. *Sci. Rep.* **10**, 4065 (2020).
- Kaushik, S. et al. Transport signatures of Fermi arcs at twin boundaries in Weyl materials. <https://doi.org/10.48550/arXiv.2207.14109> (2022).
- Mathur, N. et al. Atomically sharp internal interface in a chiral weyl semimetal nanowire. *Nano Lett.* **23**, 2695–2702 (2023).
- Winkelmann, A. et al. Kikuchi pattern simulations of backscattered and transmitted electrons. *J. Microsc.* **284**, 157–184 (2021).
- Magnéli, A. Tungstenoxides from Scheele to our times - law of constant proportions versus nonstoichiometry and structural disorder. *Chem. Scr.* **26**, 535–546 (1986).
- Magnéli, A. On heterogeneous crystalline compounds and the phasoid concept. *Microsc. Microanal. Microstruct.* **1**, 299–302 (1990).
- Svensson, G. HREM studies of intergrowth between NbO and perovskite in the Ba-, Sr and K-Nb-O systems. *Microsc. Microanal. Microstruct.* **1**, 343–356 (1990).
- Grin, Y. et al. Atomic interactions in the intermetallic catalyst GaPd. *Mol. Phys.* **114**, 1250–1259 (2016).
- Wagner F., Grin Y. *Comprehensive Inorganic Chemistry III (third edn eds Reedijk J, Poepfelmeier K)*. 222–237 (Elsevier, 2023)
- Balmes, O., Malm, J.-O., Karlsson, G. & Bovin, J.-O. Cryo-TEM observation of 3-dimensionally ordered aggregates of 5-nm gold particles in organic solvents. *J. Nanoparticle Res.* **6**, 569–576 (2004).
- Bosholm, O., Oppermann, H. & Däbritz, S. Chemischer transport intermetallischer Phasen III: das System Co-Si / chemical vapour transport of intermetallic phases III: the system Co-Si. *Z. für Naturforsch. B* **55**, 1199–1205 (2000).
- Binnewies M., Glaum R., Schmidt M., Schmidt P. *Chemical Vapor Transport Reactions* (2012).
- Blessing, R. An empirical correction for absorption anisotropy. *Acta Crystallogr. Sect. A* **51**, 33–38 (1995).
- Akselrud, L. & Grin, Y. WinCSD: software package for crystallographic calculations (Version 4). *J. Appl. Crystallogr.* **47**, 803–805 (2014).
- Sheldrick, G. Crystal structure refinement with SHELXL. *Acta Crystallogr. Sect. C* **71**, 3–8 (2015).
- Nolze, G., Hielscher, R. & Winkelmann, A. Electron backscatter diffraction beyond the mainstream. *Cryst. Res. Technol.* **52**, 1600252 (2017).
- Wang, Z. Y. et al. Epitaxial growth of core-shell zeolite X-A composites. *Crystengcomm* **14**, 2204–2212 (2012).
- Wang, Y., Salzberger, U., Srot, V., Sigle, W. & van Aken, P. A. STEM SI Warp: a Digital Micrograph script tool for warping the image distortions of atomically resolved spectrum image. *Microsc. Microanal.* **23**, 408–409 (2017).
- Koepernik, K. & Eschrig, H. Full-potential nonorthogonal local-orbital minimum-basis band-structure scheme. *Phys. Rev. B* **59**, 1743–1757 (1999).
- Perdew, J. P. & Wang, Y. Accurate and simple analytic representation of the electron-gas correlation energy. *Phys. Rev. B* **45**, 13244–13249 (1992).
- Kohout, M. Bonding indicators from electron pair density functionals. *Faraday Discuss.* **135**, 43–54 (2007).
- Ormezi, A., Rosner, H., Wagner, F. R., Kohout, M. & Grin, Y. Electron localization function in full-potential representation for crystalline materials. *J. Phys. Chem. A* **110**, 1100–1105 (2006).
- Kohout M. D. *Grid. 4.6-5.0 edn* (2018).
- Bader R. F. W., Bader R. F. *Atoms in Molecules: A Quantum Theory* (Clarendon Press, 1990).
- Kohout, M. & Savin, A. Atomic shell structure and electron numbers. *Int. J. Quant. Chem.* **60**, 875–882 (1996).

54. Grin Y. 2.13 - Crystal Structure and Bonding in Intermetallic Compounds. In: *Comprehensive Inorganic Chemistry II (Second Edition)* (eds Reedijk J., Poeppelmeier K.). (Elsevier, 2013).
55. Bende, D., Wagner, F. R. & Grin, Y. 8 - N rule and chemical bonding in main-group MgAgAs-type compounds. *Inorg. Chem.* **54**, 3970–3978 (2015).

Acknowledgements

The authors acknowledge Dr. F. R. Wagner for fruitful discussions. A.W. was supported by the Polish National Science Centre (NCN), grant No. 2020/37/B/ST5/03669.

Author contributions

M.S.: preparation of the crystals by the mCVT method; U.B.: EBSD experiment and pattern evaluation. A.W.: EBSD pattern evaluation. M.K.: preparation of cubes with 20 μm dimensions by FIB technique from polycrystalline material. H.B.: X-ray diffraction experiment as well as crystal structure solution and refinement. Y.G.: crystal structure solution and refinement; quantum chemical calculations and bonding analysis. WC-C: HR-TEM sample preparation, HR-STEM imaging and processing, HR-STEM image analysis, design of the monoclinic structure model for theoretical calculation. P.S.: HR-TEM imaging, HR-STEM image analysis

Funding

Open Access funding enabled and organized by Projekt DEAL.

Competing interests

The authors declare no competing interests

Additional information

Supplementary information The online version contains supplementary material available at <https://doi.org/10.1038/s43246-023-00434-8>.

Correspondence and requests for materials should be addressed to Ulrich Burkhardt.

Peer review information Communications Materials thanks Weiwei Xie and the other, anonymous, reviewer(s) for their contribution to the peer review of this work. Primary Handling Editors: Andreja Benčan Golob and Aldo Isidori.

Reprints and permission information is available at <http://www.nature.com/reprints>

Publisher's note Springer Nature remains neutral with regard to jurisdictional claims in published maps and institutional affiliations.



Open Access This article is licensed under a Creative Commons Attribution 4.0 International License, which permits use, sharing, adaptation, distribution and reproduction in any medium or format, as long as you give appropriate credit to the original author(s) and the source, provide a link to the Creative Commons license, and indicate if changes were made. The images or other third party material in this article are included in the article's Creative Commons license, unless indicated otherwise in a credit line to the material. If material is not included in the article's Creative Commons license and your intended use is not permitted by statutory regulation or exceeds the permitted use, you will need to obtain permission directly from the copyright holder. To view a copy of this license, visit <http://creativecommons.org/licenses/by/4.0/>.

© The Author(s) 2023